5.1. Characterization of Gadolinium doped iron oxide nanoparticles (metallic core).

5.1.1. Transmission electron microscopy (TEM).

The study was performed for visualization of morphology of metallic nanoparticles and to analyse the true particle size. It was performed on transmission electron microscope, JEOL, JEM-2100, Japan with voltage acceleration of 200kV and suitable magnification (1, 2).

5.1.2. Zeta Potential.

The zeta potential of the metallic core synthesized by the polyol process and carboxylated metallic core were subjected to measurement of zeta potential by Doppler anemometry using Zeta Sizer, Nano ZS, Malvern instruments, UK. The undiluted samples were filled in electrode capillary cuvette prior to the measurement (3, 4).

5.1.3. *In vitro* MRI contrast.

In vitro MRI contrast study was performed to optimise the precursor ratio of Gadolinium and iron in the synthesis. The MRI phantoms of gelatin blocks were prepared using solvent casting a with the composition given in table 5.1 and were casted in 8.3x5.3x0.8 cm (length x breadth x thickness) dimension using a plastic mould to mimic the biological tissue (5). The metallic nanoparticles were prepared in ratios of 1:10, 1:7.5 and 1:5 (Gd: Fe precursor) along with controls of pure iron oxide and gadolinium oxide nanoparticles with the optimised conditions of the polyol process described in previous chapter. The synthesized nanoparticles were dispersed in deionised water in concentration of 5mg/ml and filled in different syringes with 26 gauze needle. In the process of casting of gelatin blocks the metallic nanoparticles (5mg/ml) were injected before the solidification of gelatin after pouring the hot mix in the casting trays as shown in figure 5.1. After the solidification of gelatin blocks, they were subjected to magnetic resonance imaging (MRI) in T1 (light) and T2 modes(dark) using a 1.5T clinical MRI machine, Signa, GE healthcare, India (6).

Table 5.1: Composition of gelatin MRI phantoms.

Ingredient	Role	Quantity
Gelatin (Microbiology grade)	Matrix former	30%w/v
Polyhexamethylene biguanide (20%)	Preservative	0.2ml
Double distilled water	Solvent	Upto 30ml

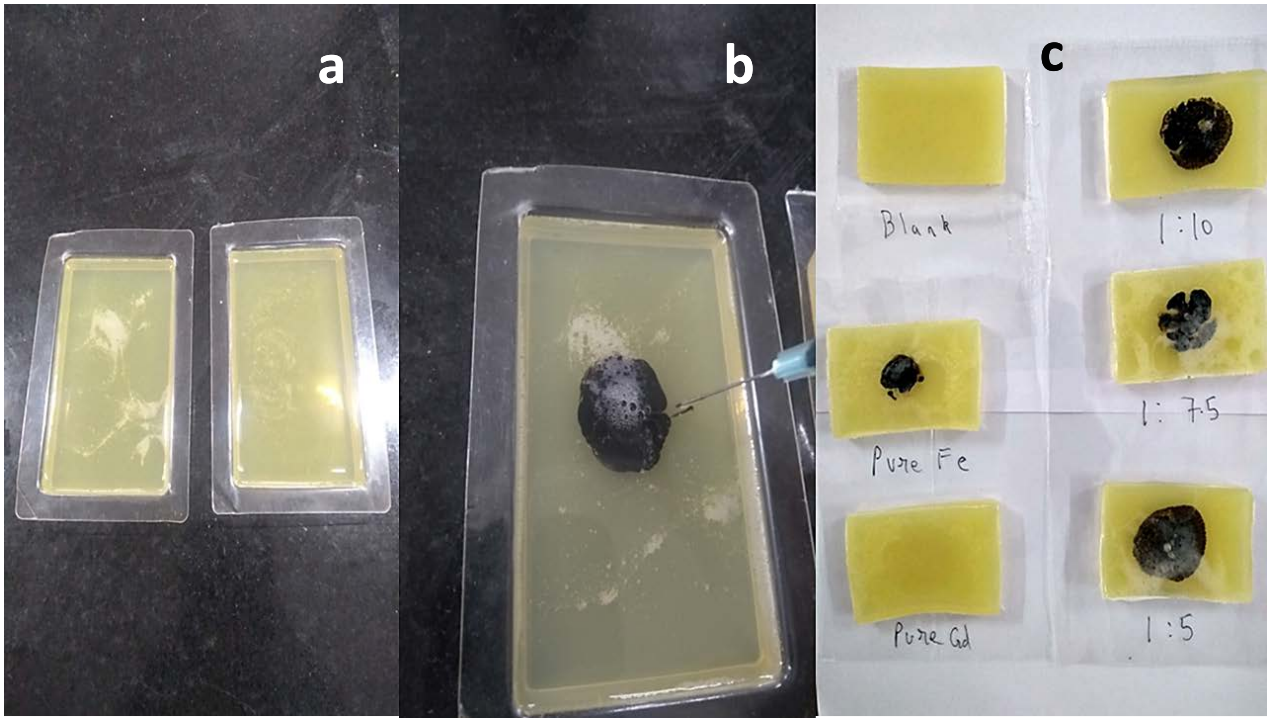

Figure 5.1: (a) Casting of gelatin blocks as MRI phantoms, (b) Impregnation of metallic nanoparticles in gelatin blocks and (c) Gelatin blocks with controls and samples.

5.1.4. Energy dispersive X- ray diffraction (EDAX).

The elemental composition was determined through analysis performed using EDAX, Xmax, Oxford instruments, UK. The Gd doped iron oxide nanoparticles were exposed to X-rays of mid energy (1-20KeV) which were collected by the detector for qualitative as well as quantitative estimation of elements present in the sample (7-9).

5.1.5. X-ray diffraction (XRD).

The X-ray diffraction patterns were recorded for the samples of gadolinium doped iron oxide nanoparticles, Iron oxide nanoparticles and gadolinium oxide nanoparticles synthesized by polyol method at 2θ values of 20 °to 100° with generator parameters of 40 mA, 45 kV using PANalytical X'Pert Pro, Malvern Instruments, UK (10-12) .

5.1.6. Vibrating sample magnetometry (VSM).

The magnetic behaviour of the gadolinium doped iron oxide, plain iron oxide and gadolinium oxide nanoparticles was studied using vibrating sample magnetometer Lakeshore VSM, 7410,USA.The hysteresis curves were recorded at room temperature with respect to varying magnetic field (13-15).

5.1.7. *In vitro* hyperthermia.

The ability of the Gadolinium doped iron oxide nanoparticles to elevate the surrounding temperature in presence of alternating magnetic field of 516 and 714 kHz at 20mT magnetic field was done using magneTherm™ system, nano Therics, UK. The rise in temperature was recorded with respect to time (16-18).

5.2. Characterization of theranostic nanoparticles .

5.2.1. Differential scanning calorimetry (DSC).

It was performed for the samples of lenanidomide, PLGA, PVA, Gadolinium doped iron oxide nanoparticles, PEI-FA-TPP, their physical mixture, and lyophilised theranostic nanoparticles to check the compatibility of the drug, polymer and the metallic core and to determine whether the drug is physically adsorbed or entrapped on the metallic core. The samples were subjected to thermal analysis from temperatures of 30-300°C with 10°C/min ramping rate under nitrogen purged atmosphere using DSC-60, Shimadzu, Japan (19, 20).

5.2.2. Particle size and zeta potential.

1 ml of the dispersion of theranostic nanoparticle was diluted suitably with double distilled water to measure particle size using dynamic light scattering technique while zeta potential was determined for the undiluted sample in electrode capillary cell using doppler anemometry technique using Zeta Sizer, Nano ZS, Malvern Instruments, UK (21, 22).

5.2.3. Transmission electron microscopy (TEM).

The study was performed for visualization of morphology of theranostic nanoparticles and to analyse the true particle size. It was performed on transmission electron microscope, JEOL, JEM-2100, Japan with voltage acceleration of 200kV and suitable magnification (23, 24).

5.2.4. % Entrapment efficiency.

The drug entrapped in the PLGA coat over the magnetic core was determined by using UV spectroscopy.1ml of nanoparticulate dispersion of the final formulation was taken and was centrifuged at 2000 rpm for 10 mins using REMI, C-24 plus centrifuge, India. The supernatant was separated from residue (free drug) and treated with Acetonitrile: Methanol (1:1) to extract the entrapped drug with sonication for 3 minutes. After sonication the sample was centrifuged to 15000 rpm for 10 mins to get clear solution for analysis at 310nm using UV spectrophotometer, UV 1800, Shimadzu, Japan (25). The % entrapment efficiency was calculated as per the following equation

$$\%\ Entrapment = \frac{Drug\ extracted\ from\ supernatant}{total\ drug\ added} x100$$

5.2.5. Gas chromatography.

The headspace analysis of the theranostic nanoparticles was done for estimation of acetone content as residual solvent using gas chromatography, GC 606, Sigma Instruments, India. The standard of 10ppm of acetone was used to compare the area of the peak with the sample of theranostic nanoparticles (26).

5.2.6. *In vitro* drug release.

For the study dialysis sac method was used consisting of a dialysis bag (MWCO. 12000, pore size 2.4nm, Himedia, India) which was activated prior to use and filled with drug suspension/drug coated core /theranostic nanoparticles equivalent to 1 mg of drug after which bag was tied properly, avoiding leakage and was place in a beaker filled with 30 ml of Phosphate buffer saline + 10 % methanol which acted as receptor compartment.

The contents of the receptor compartment were stirred at 100±10 rpm and 37±0.5°C to facilitate diffusion from which 1 ml samples were withdrawn at specific time intervals and replaced with fresh buffer to maintain sink condition. The withdrawn samples were analysed at 302nm using UV spectrophotometer, UV-1800, Shimadzu, Japan (27-29).

5.2.7. Stability study.

The theranostic nanoparticles were kept at Room temperature (30±5°C, 65±5%RH) and at refrigerated conditions (2-8°C) in polypropylene tubes for a period of 30 days and the samples were withdrawn at the interval of 10 days and were analysed for the particle size and the drug content (30).

5.3. Results and discussion.

5.3.1. Characterization of Gadolinium doped iron oxide nanoparticles (metallic core).

5.3.1.1. Transmission electron microscopy.

The transmission electron microscopy showed the spherical morphology of the nanoparticles with particle size lower than 10nm as shown in figure 5.2 (a). The crystalline lattice can be visualised from the high resolution image of the Gd doped iron oxide nanoparticles in figure 5.2 (b). The TEM analysis revealed the true particle size which is always lower than the particle size determined by dynamic light scattering technique where the layer of the dispersant medium is added to the diameter of the particles (31, 32).

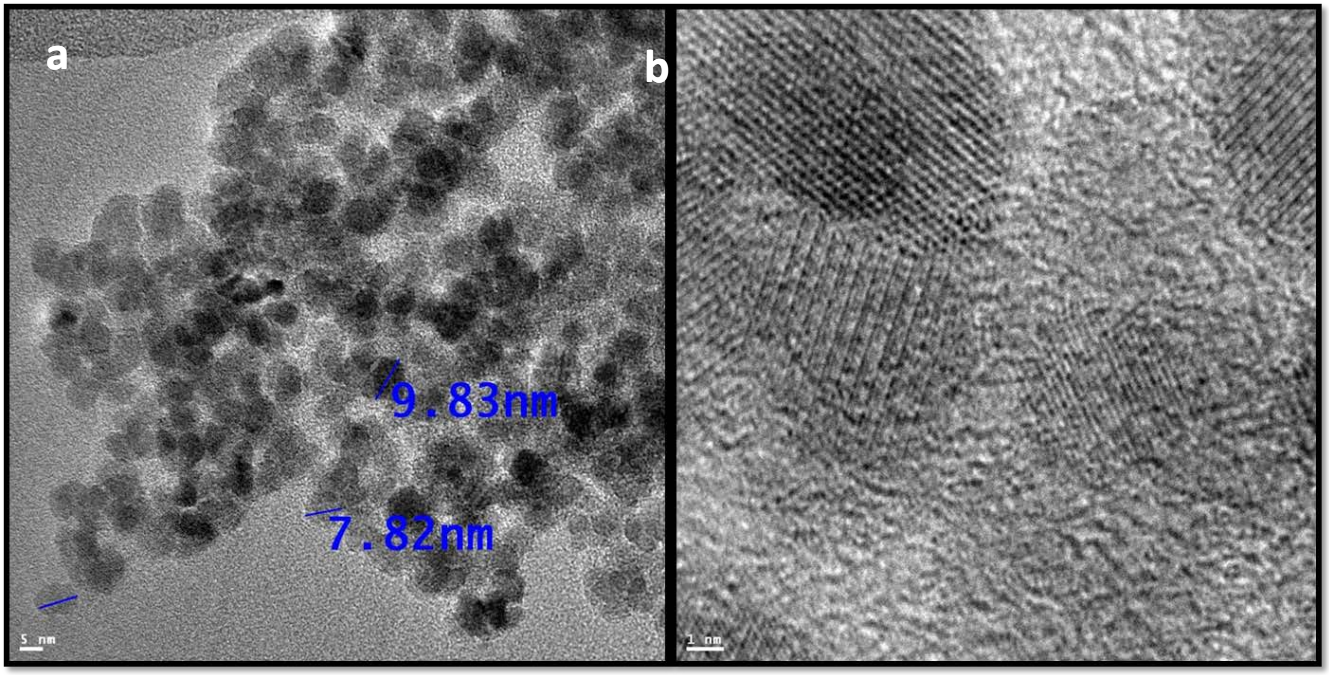

Figure 5.2: (a) TEM analysis of metallic core (b) high resolution image of metallic core.

5.3.1.2. Zeta potential.

The zeta potential of the metallic core after polyol synthesis was found to be 31.56±4.53mV due to the adsorption of tetraethylene glycol on the metallic core as it acts as a capping agent for the metallic nanoparticles during the synthetic phase of polyol process and limits the particle size growth (33).

The zeta potential of citrate functionalised metallic core was found to be -22.3±3.85mV due to anchoring of carboxylic acid on the metallic core (34).

5.3.1.3. *In vitro* MRI contrast.

The images generated by the MRI are shown in figure 5.3. It can be seen from figure 5.3 (a) and (d) that the gelatin phantoms do not show any contrast in T1 and T2 mode. In case of pure iron oxide nanoparticles, the dark contrast is seen in figure 5.3(e) as iron oxide is a T2 contrast agent while pure gadolinium oxide nanoparticles showed light contrast as gadolinium oxide and chelates are T1 contrast agents (35, 36). In case of Gd doped iron oxide nanoparticles, dual contrast is observed in case of Gd:Fe precursors in the ratio of 1:5. The figure 5.3(c) showed light contrast (T1) which is comparable with pure gadolinium nanoparticles while the figure 5.3(f) exhibited dark contrast (T2) which is comparable with pure iron oxide nanoparticles. The ability of the dual contrast depends on the ratio of iron and gadolinium precursors. Lower ratios of gadolinium do not show adequate T1 contrast but show T2 contrast due to abundance of iron (37, 38). Thus it can be concluded that the optimised nanoparticles is having adequate dual contrast and can be used in MRI imaging.

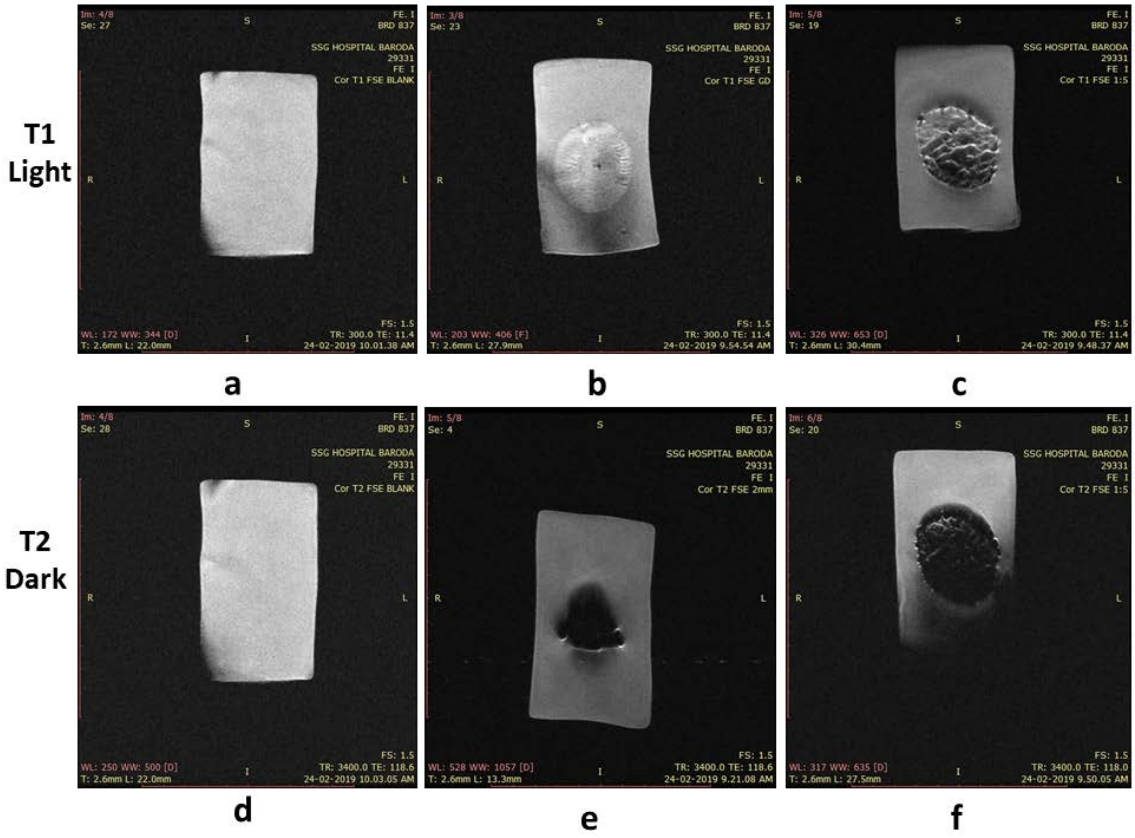

Figure 5.3: MRI images in T1 (light) mode (a) blank gelatin phantom (b) gadolinium oxide nanoparticles (c) Gd doped iron oxide nanoparticles and T2 (dark) mode (d) blank gelatin phantom (e) Iron oxide nanoparticles (f) Gd doped iron oxide nanoparticles.

5.3.1.2. Energy dispersive X- ray diffraction (EDAX).

The EDAX analysis is a qualitative and quantitative tool for the elemental analysis. The Gd doped iron oxide nanoparticles show both iron and gadolinium in the spectrum as shown in figure 5.4 and table 5.2 which displays the quantitative results of the analysis. The metallic nanoparticles show doping of gadolinium on the iron oxide (39, 40).

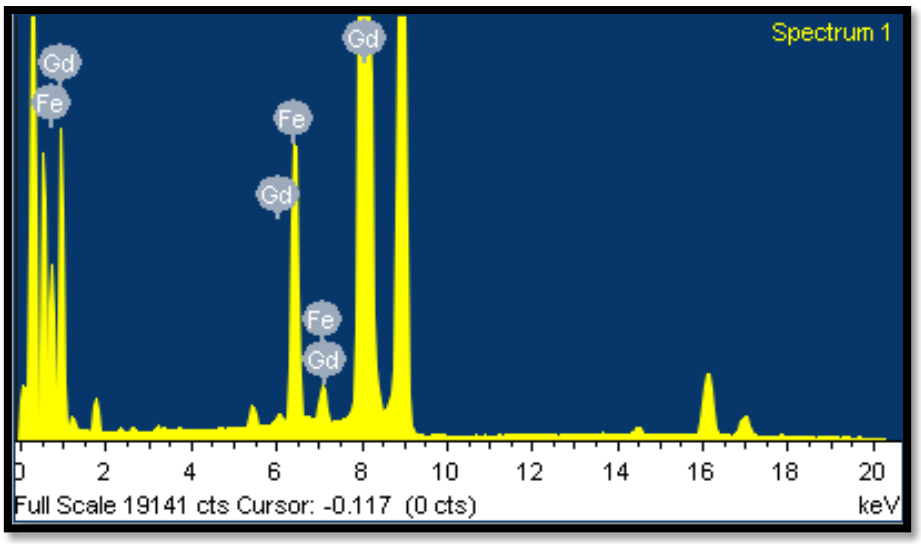

Figure 5.4: EDAX analysis spectrum of metallic nanoparticles.

Table 5.2: Quantitative results of EDAX analysis of metallic nanoparticles.

Element	Weight %	Atomic %
Fe K	94.45	97.96
Gd L	5.55	2.04
Total	100.00	

5.3.1.3. X-ray diffraction (XRD).

The results of XRD are shown in figure 5.5 and table 5.3 which show that the iron oxide nanoparticles exhibit highest crystallinity with 14.016% while the gadolinium oxide nanoparticles showed 4.250% crystallinity which was the lowest. The crystallinity of gadolinium doped iron oxide was found to be 6.923% which is due to doping of gadolinium in iron oxide crystalline lattice. The iron oxide nanoparticles show characteristic peaks at 2θ values of 30.0837, 35.5090 and 62.7553 which are visible in gadolinium doped iron oxide along with additional peaks of gadolinium oxide which suggest modification of the crystal lattice due to incorporation of gadolinium.

It can be concluded that the Fe3O4 crystals have been formed with Gd doping from the results which is in correspondence with the results of EDAX (41, 42).

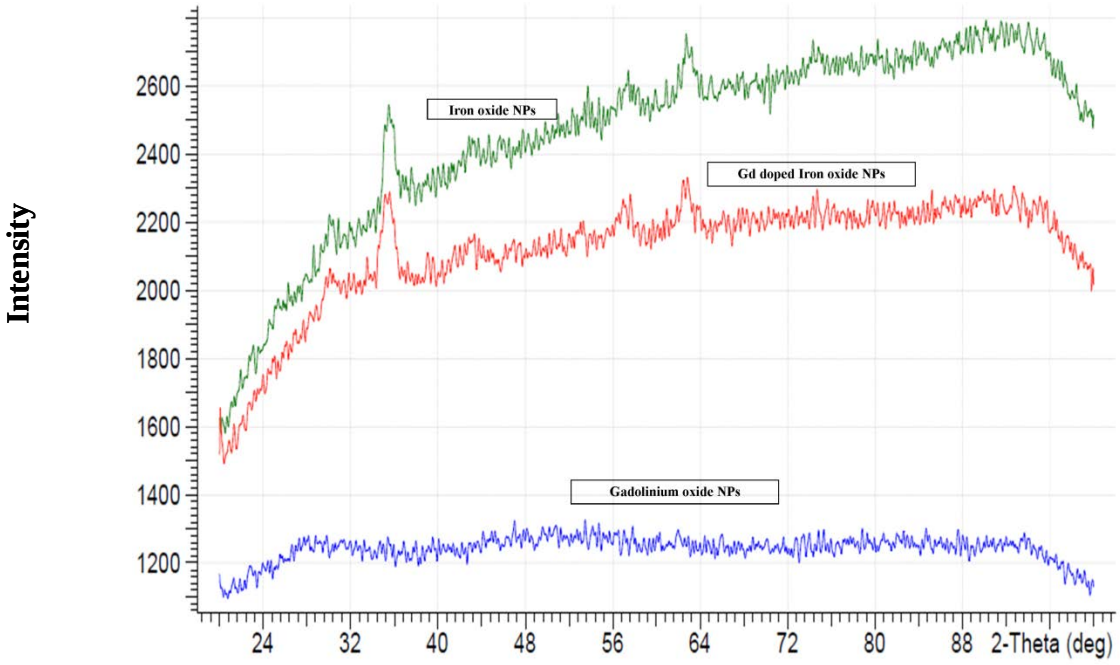

Figure 5.5: XRD diffractograms of iron oxide, gadolinium doped iron oxide and gadolinium oxide nanoparticles.

Table 5.3: Analysis of XRD peaks of iron oxide, gadolinium doped iron oxide and gadolinium oxide nanoparticles.

Iron oxide nanoparticles				
Position [°2θ]	**FWHM Total [°2θ]**	**d-spacing [Å]**	**Relative Intensity. [%]**	**Area [cts*°2θ]**
30.0837	0.8398	2.96812	33.86	68.28
35.5090	0.9254	2.52608	100.00	210.02
62.7553	0.7581	1.47942	52.21	96.15

Gadolinium doped iron oxide nanoparticles				
Position [°2θ]	**FWHM* Total [°2θ]**	**d-spacing [Å]**	**Relative Intensity [%]**	**Area [counts*°2θ]**
30.0427	1.0305	2.97207	45.66	99.37
35.3097	0.2277	2.53987	64.19	41.02
43.1785	0.0871	2.09349	34.14	7.08
53.2821	0.0660	1.71789	21.38	1.98
62.6293	0.8435	1.48209	57.49	80.56
74.6883	0.0703	1.26986	100.00	11.00
92.7704	0.1946	1.06396	31.49	17.20
***Full width at half maximum**				
% Crystallinity (Calculated using ACD spectrus processor 2020.1.2,ACD labs)				
Iron oxide	**Gadolinium doped Iron oxide**		**Gadolinium oxide**	
14.016%	6.923%		4.250%	

5.3.1.4. Vibrating sample magnetometry (VSM).

The hysteresis curves of VSM for the nanoparticles are shown in figure 5.6. It can be seen that the iron oxide nanoparticles (Fe) and gadolinium doped nanoparticles (Fe-Gd) showed paramagnetic behaviour with saturation magnetization values of 55.187 and 41.35 emu/g respectively. The gadolinium oxide nanoparticles (Gd) showed no magnetization.

The decrease of saturation magnetization in case of gadolinium doped iron oxide as compared to plain iron oxide is due to gadolinium doping. The paramagnetic behaviour with high saturation magnetization is preferred for clinical applications of MRI imaging as well as passive targeting (43, 44).

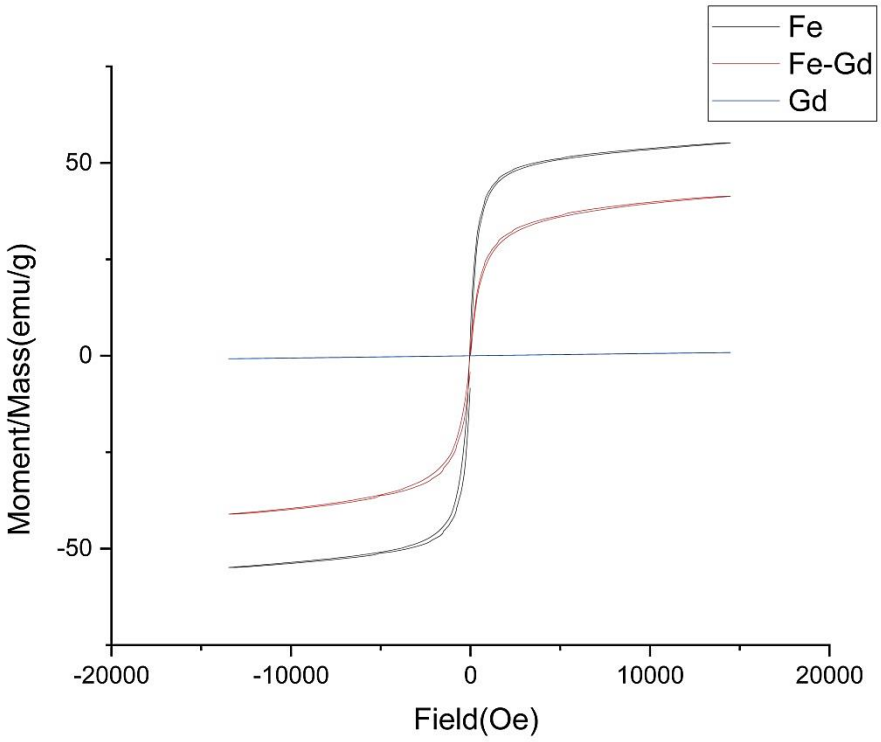

Figure 5.6: Hysteresis loops of metallic nanoparticles at room temperature.

5.3.1.5. *In vitro* hyperthermia.

The in vitro hyperthermia can be considered as a synergistic characteristics of iron oxide based nanoparticles which is useful for treatment of cancer as cancerous cells have low survival at high temperatures exceeding 40°C. The result of the experiment can be seen in figure 5.7. In case of 5mg/ml of the Gd doped iron oxide nanoparticles at 516kHz of alternating magnetic field, the time required to raise the temperature above 40°C was found to be 12.95 minutes while at 744kHz it was 1.83 minutes. In case of 10mg/ml of the nanoparticles at 516kHz, it was found to be 2.3 minutes and at 744 kHz it was 2.8 minutes to raise the temperature above 40°C.

It can be concluded that the concentration of 5mg/ml of the nanoparticles at 744 kHz is having the lowest time of 1.83 minutes which is preferable as it shortens the exposure period to the magnetic field and can reduce the toxicity due to exposure of the metallic nanoparticles in the target region (45, 46).

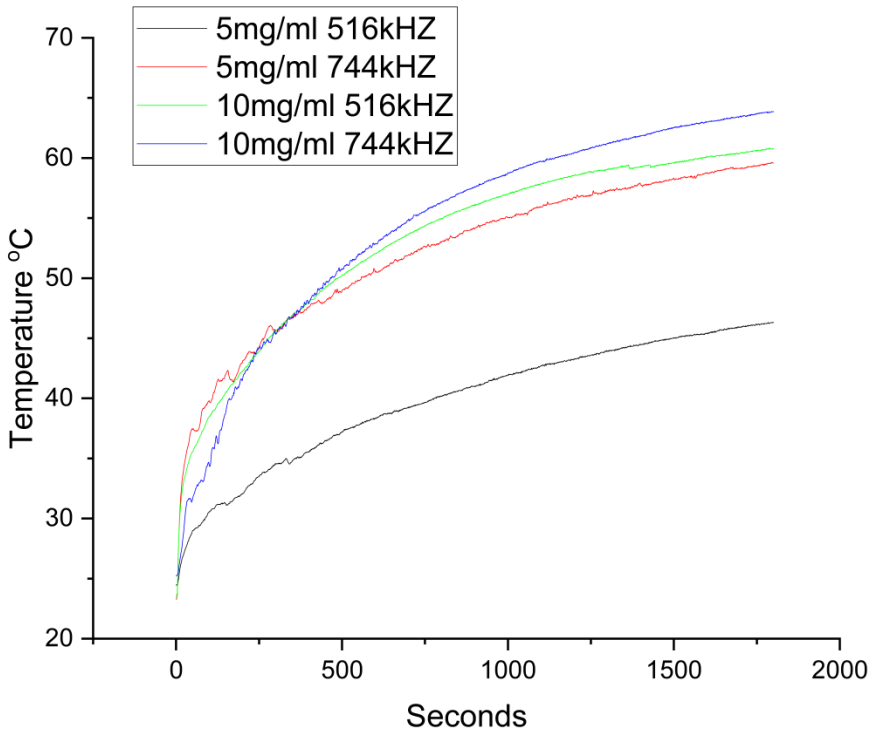

Figure 5.7: Temperature curves for metallic nanoparticles exposed to alternating magnetic field.

5.3.2. Characterization of theranostic nanoparticles.

5.3.2.1. Differential scanning calorimetry (DSC).

This technique is used to assess compatibility of the ingredients of the formulation and their interactions if any are present. As shown in figure 5.8, the thermogram of lenalidomide exhibits a sharp endothermic peak at 270.01°C which is due to melting point of drug. Presence of small endothermic peak at 50.1°C is characteristic glass transition of PLGA. PVA showed a small endotherm at 166.62°C while Gd doped iron oxide NPs do not display any specific peak due to high melting point of iron oxide. PEI-FA-TPP showed broad endotherm at 158.06°C which indicated melting of the polymer. The physical mixture exhibited a sharply visible endothermic peak at 265.66°C which corresponded to the peak of lenalidomide which suggested that there is no physical or chemical interaction between the drug and the ingredients of the formulation. Thermogram of drug loaded theranostic nanoparticles showed no peak of drug which directed that the drug is completely encapsulated inside and not adsorbed on the polymeric coat (47).Small peak at 149.19°C is due to the secondary PEI-FA-TPP coating.

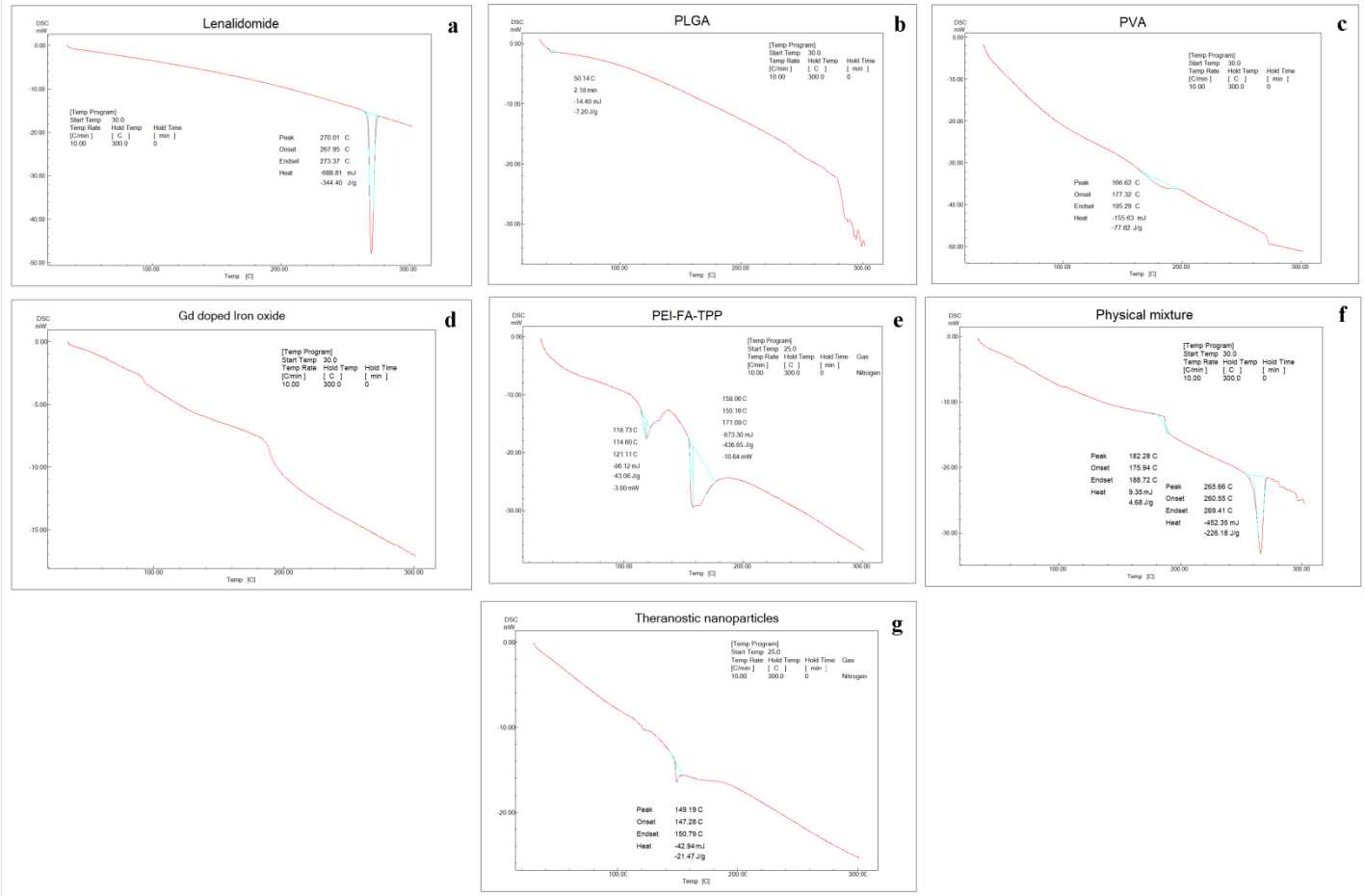

Figure 5.8: Thermograms of (a) Drug, (b) PLGA, (c) PVA, (d) Gd doped iron oxide, (e) Physical mixture, (f) PEI-FA-TP and (g) Theranostic nanoparticles.

5.3.2.2. Particle size and zeta potential.

The particle size of the theranostic nanoparticles was found to found to be 122.26±2.17 nm with PDI of 0.161±0.009. The particle size of the theranostic nanoparticles is less than 200 nm which is suitable for delivery to the CNS and the low PDI indicates the sample is relatively monodisperse (48). The zeta potential of theranostic nanoparticles was found to be 12.3±0.52 mV which is due to the unmodified amines present in the PEI polymer which induce the positive charge (49).

5.3.2.3. Transmission electron microscopy (TEM).

The TEM image as shown in figure 5.9 shows the nanoclusters of polymeric coated metallic nanoparticles which are semi spherical shaped and have a light corona around the nanoparticles due to coating of polymer.

The particle size analysed by TEM is lower than that determined by dynamic light scattering as in case of TEM, particles are analysed in dehydrated state and there is no layer of the dispersant media around the nanoparticles (50).

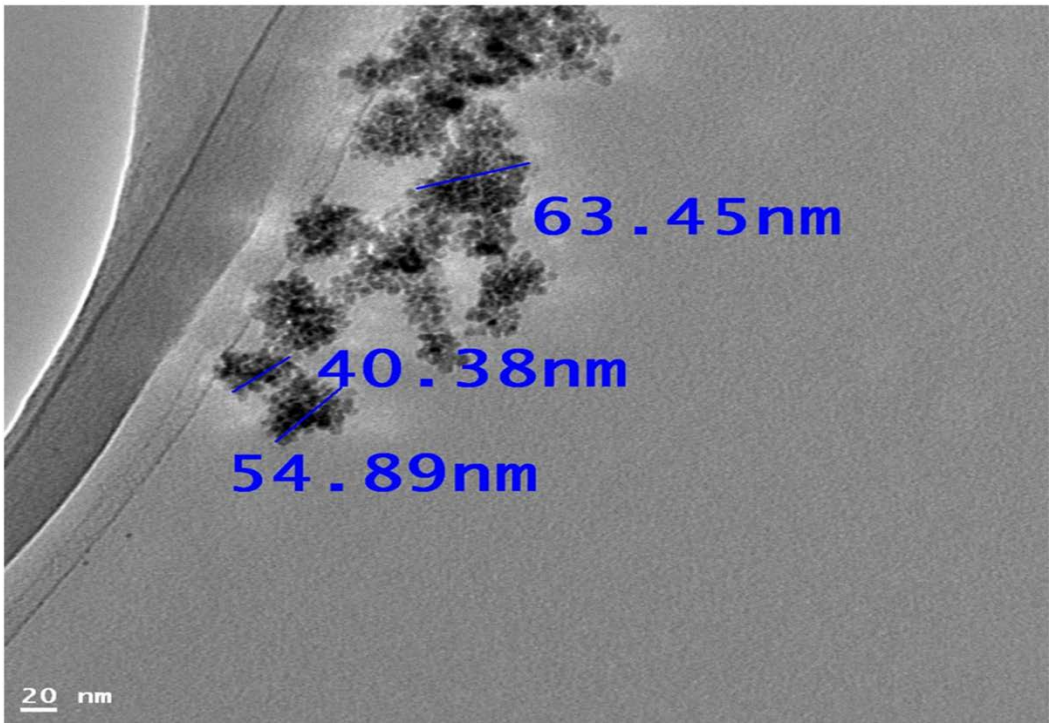

Figure 5.9: TEM analysis of theranostic nanoparticles.

5.3.2.4. % Entrapment efficiency.

The % entrapment efficiency for the theranostic nanoparticles was found to be 97.49±0.42 which is due to the hydrophobic characteristic of the drug lenalidomide as hydrophobic drugs show high entrapment with nanoprecipitation technique in which hydrophobic polymer PLGA is used. (51, 52).

5.3.2.5. Gas chromatography.

The organic solvent acetone used in the process of polymeric coating on the metallic core can cause toxicity if the process parameters are inappropriate resulting in partial removal of the organic solvent by means of evaporation. The figure 5.10 shows the curve peak of standard of acetone of 10ppm and the headspace analysis of the theranostic nanoparticles.

The amount of the residual solvent (acetone) in the theranostic nanoparticles was found to be 1.480 ppm which is less than the daily exposure limit of 5000 ppm as per the ICH guideline Q3C (R6) on impurities: guideline for residual solvents (53).

Thus it can be concluded that the process used for the coating of nanoparticles is efficient in removal of the organic phase from the dispersion.

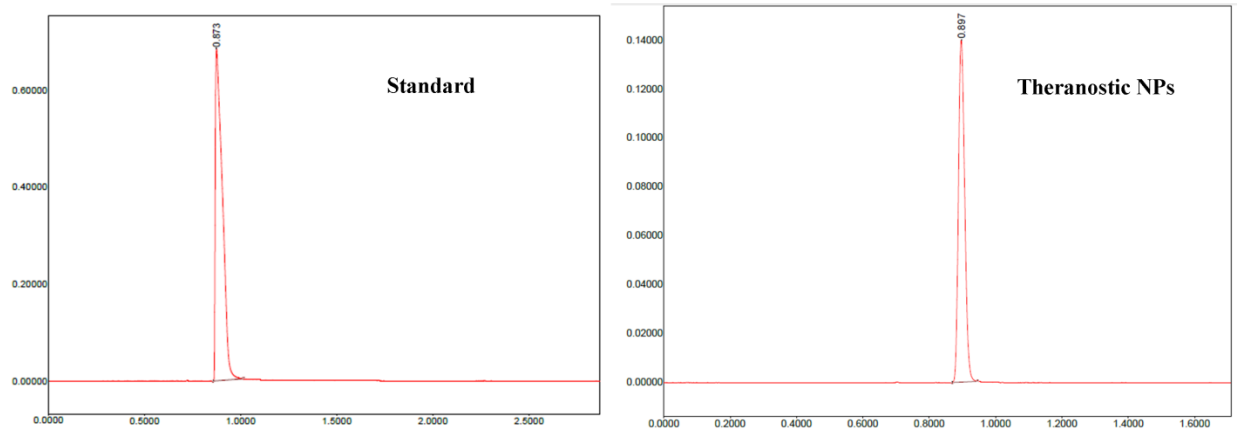

Figure 5.10: Gas chromatograms of standard and theranostic nanoparticles for acetone detection as residual solvent.

Table 5.4: Analysis of peak area of GC for residual solvent analysis.

Sr.no	Sample	RT(min)	Area(mV*sec)
1	Acetone standard 10 ppm	0.873	1755.731
2	Theranostic nanoparticles	0.897	184.150

5.3.2.6. *In vitro* drug release.

The drug release is dependent on the type of nanoparticle or system which can be either monolithic or core-shell type of system as shown in figure 5.11.

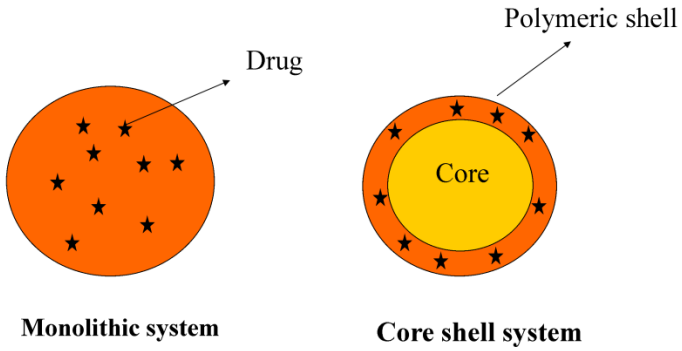

Figure 5.11: Comparison of matrix and core shell type of systems.

The mathematical models have been established for prediction of drug release from such systems. In case of monolithic systems the release kinetics can be understood from the equation given below (54).

$$\frac{dm}{dt} = -AP(C - C\infty)$$

dm/dt=rate of drug release.

A=surface area.

P=permeability of drug.

C-C∞=concentration gradient.

It can be understood from the above equation that the release of drug is due to the change in surface area due to the erosion/hydrolysis of polymeric matrix.

In case of the core shell systems where the coating of shell is few nanometers thick the equation for the drug release is given below(54).

$$\frac{dm}{dt} = -Ah(C - C\infty)$$

Here,

dm/dt=rate of drug release.

A=surface area.

h=convection coefficient of external medium

C-C∞=concentration gradient.

Here drug release is dependent on the change in surface area due to polymeric erosion/hydrolysis and convection factor that is the movement of external medium which induces concentration gradient (54). The composition of the external medium also affects the convection factor. In case of theranostic nanoparticles the coating of the polymer is having low thickness as shown in figure 5.12(a), where the core is surrounded by a thin layer of polymeric coat.

The figure 5.12(b) shows the release profile of the pure drug suspension, drug coated core and theranostic nanoparticles in methanolic phosphate buffer saline pH 7.4.

It can be seen that the drug release of pure drug suspension was found to be 96.28±2.43% in 2 hours while the drug coated core and theranostic nanoparticles showed 97.54±2.01% 95.18±3.50% in 8 hours respectively.

In case of the drug coated core and theranostic nanoparticles the drug release is accelerated due to the enhanced dissolution of the drug in hydroalcoholic mixture of methanol and buffer which enhances convection factor and the sink conditions maintained the concentration gradient (55). It can be also hypothesized that the exposure of magnetic field from the magnetic stirrer used in the experiment can cause disruption of the polymeric shell due to the behaviour of iron oxide nanoparticles under the influence of magnetic field thereby accelerating the drug release. Pulsatile release of drugs under the influence of magnetic field have been investigated with PLGA coated iron oxide nanoparticles and microspheres (56-58).

The release kinetics was determined in each case by regression equation obtained from various fit models. It was found that the pure drug suspension followed Korsmeyer Peppas model with regression coefficient of 0.995. The intercept value of the regression equation further explains the release mechanism in this model. It was found that the pure drug suspension had intercept value of 0.7146 which indicates non fickian diffusion (0.5<intercept value<1). The drug coated metallic core followed Hixon Crowell model with regression coefficient of 0.9785 which indicates that the drug release is due to the layer by layer erosion of polymeric coat. In case of theranostic nanoparticles first order release kinetics were obeyed with regression coefficient of 0.9934 which is observed in core shell systems (59, 60).

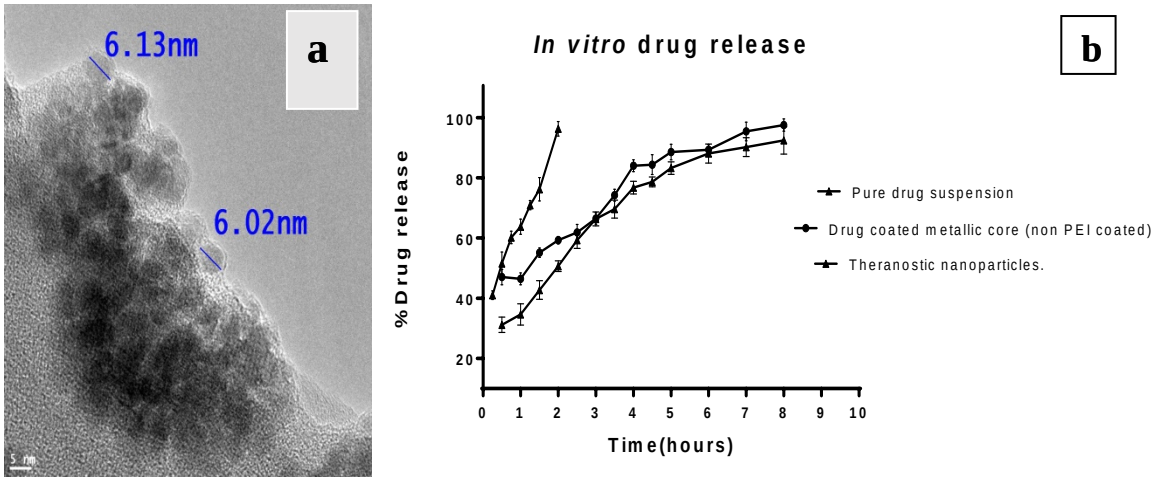

Figure 5.12 (a) TEM image showing polymeric coat thickness over theranostic nanoparticles. (b) Comparison of *In vitro* drug release profile of drug suspension, drug coated core and theranostic nanoparticles (n=3).

Table 5.4: Release kinetics of Plain drug suspension, drug coated core and theranostic nanoparticles.

	Regression coefficient(r^2)		
Release model	**Plain drug suspension**	**Drug coated core**	**Theranostic nanoparticles**
Zero order	0.9843	0.9324	0.9086
First order	0.8105	0.9569	0.9934
Higuchi	0.9628	0.9324	0.9711
Hixon Crowell	0.8923	0.9785	0.9798
Korsmeyer Peppas	0.995	0.8969	0.9751

5.3.2.7. Stability study.

The results of stability study are shown in figure 5.13 which indicate that theranostic nanoparticles showed a significant increase in particle size at room temperature from 124.29±2.83 nm to 159.36±0.20nm after a period of 30 days while in case of refrigerated temperature of 2-8°C retarded the increase of particle. The results can be attributed to the PLGA used in the polymeric shell. The polymer undergoes hydrolysis when it comes in contact with the aqueous medium due to breakage of ester bonds. The pores are generated and the polymeric chain mobilization causes the increase in the particle size along with surface erosion of the polymeric coat (61-63).

The % assay remained unaffected due to the stability of the drug in both the storage conditions and no degradation mechanism of drug has been reported in aqueous medium (64).

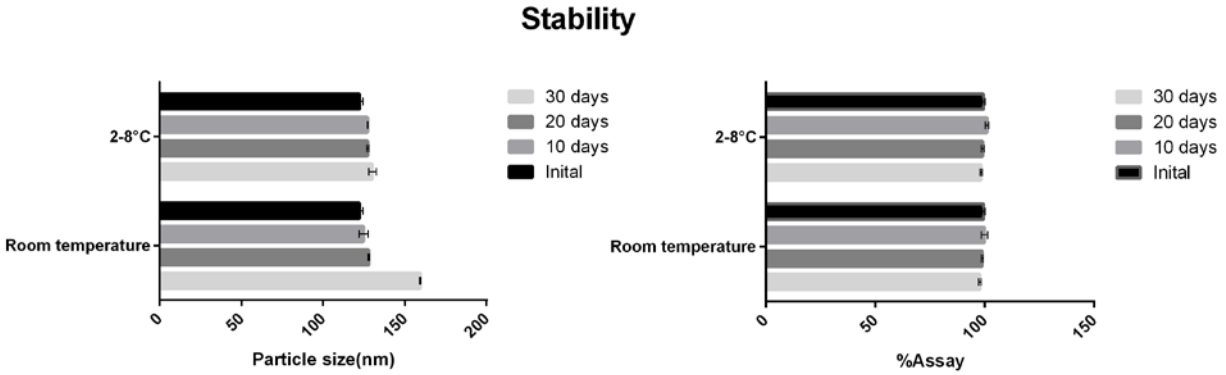

Figure 5.13: Results of stability study at room temperature and refrigerated conditions.

5.4. References

1. Schwaminger SP, Syhr C, Berensmeier S. Controlled synthesis of magnetic iron oxide nanoparticles: Magnetite or maghemite? Crystals. 2020;10(3):214.
2. Sharma P, Holliger N, Pfromm PH, Liu B, Chikan V. Size-Controlled Synthesis of Iron and Iron Oxide Nanoparticles by the Rapid Inductive Heating Method. ACS omega. 2020;5(31):19853-60.
3. Cardoso RM, Deda DK, Toma SH, Baptista MS, Araki K. Beyond electrostatic interactions: ligand shell modulated uptake of bis-conjugated iron oxide nanoparticles by cells. Colloids and Surfaces B: Biointerfaces. 2020;186:110717.
4. Gupta PK, Dravid VP, De M. Ultrathin Silica-Coated Iron Oxide Nanoparticles: Size-Property Correlation. ChemistrySelect. 2020;5(29):8929-34.
5. Fieremans E, De Deene Y. Gel Phantoms for Diffusion MRI Studies. NMR and MRI of Gels2020. p. 379-400.
6. Athar T, Vishwakarma SK, Bardia A, Khan AA. Super paramagnetic iron oxide and gadolinium (FeGdO3) nanopowder synthesized by hydrolytic approach passes high level of biocompatibility and MRI-based dual contrast property for competent molecular imaging and therapeutic interventions. Biomedical Physics & Engineering Express. 2016;2(2):025010.
7. Scimeca M, Bischetti S, Lamsira HK, Bonfiglio R, Bonanno E. Energy Dispersive X-ray (EDX) microanalysis: A powerful tool in biomedical research and diagnosis. European journal of histochemistry: EJH. 2018;62(1).
8. Mahdavi M, Ahmad MB, Haron MJ, Namvar F, Nadi B, Rahman MZA, et al. Synthesis, surface modification and characterisation of biocompatible magnetic iron oxide nanoparticles for biomedical applications. Molecules. 2013;18(7):7533-48.
9. Rahman SSU, Qureshi MT, Sultana K, Rehman W, Khan MY, Asif MH, et al. Single step growth of iron oxide nanoparticles and their use as glucose biosensor. Results in Physics. 2017 2017/01/01/;7:4451-6.
10. Besenhard MO, LaGrow AP, Hodzic A, Kriechbaum M, Panariello L, Bais G, et al. Co-precipitation synthesis of stable iron oxide nanoparticles with NaOH: New insights and continuous production via flow chemistry. Chemical Engineering Journal. 2020 2020/11/01/;399:125740.
11. Abdel Aziz WN, Bumajdad A, Al Sagheer F, Madkour M. Selective synthesis and characterization of iron oxide nanoparticles via PVA/PVP polymer blend as structure-directing agent. Materials Chemistry and Physics. 2020 2020/07/15/;249:122927.
12. Laid TM, Abdelhamid K, Eddine LS, Abderrhmane B. Optimizing the biosynthesis parameters of iron oxide nanoparticles using central composite design. Journal of Molecular Structure. 2020 2020/10/20/:129497.
13. Mansur S, Rai A, Holler RA, Mewes T, Bao Y. Synthesis and characterization of iron oxide superparticles with various polymers. Journal of Magnetism and Magnetic Materials. 2020 2020/12/01/;515:167265.
14. Ounacer M, Essoumhi A, Sajieddine M, Razouk A, Costa BFO, Dubiel SM, et al. Structural and Magnetic Studies of Annealed Iron Oxide Nanoparticles. Journal of Superconductivity and Novel Magnetism. 2020 2020/10/01;33(10):3249-61.
15. Kuciakowski J, Kmita A, Lachowicz D, Wytrwal-Sarna M, Pitala K, Lafuerza S, et al. Selective magnetometry of superparamagnetic iron oxide nanoparticles in liquids. Nanoscale. 2020;12(31):16420-6.
16. Soleymani M, Velashjerdi M, Shaterabadi Z, Barati A. One-pot preparation of hyaluronic acid-coated iron oxide nanoparticles for magnetic hyperthermia therapy and targeting CD44-overexpressing cancer cells. Carbohydrate Polymers. 2020 2020/06/01/;237:116130.
17. Dadfar SM, Camozzi D, Darguzyte M, Roemhild K, Varvarà P, Metselaar J, et al. Size-isolation of superparamagnetic iron oxide nanoparticles improves MRI, MPI and hyperthermia performance. Journal of Nanobiotechnology. 2020 2020/01/28;18(1):22.

18. Kowalik P, Mikulski J, Borodziuk A, Duda M, Kamińska I, Zajdel K, et al. Yttrium-Doped Iron Oxide Nanoparticles for Magnetic Hyperthermia Applications. The Journal of Physical Chemistry C. 2020 2020/03/26;124(12):6871-83.
19. Hedayatnasab Z, Dabbagh A, Abnisa F, Wan Daud WMA. Polycaprolactone-coated superparamagnetic iron oxide nanoparticles for in vitro magnetic hyperthermia therapy of cancer. European Polymer Journal. 2020 2020/06/15/;133:109789.
20. Mohammadi G, Namadi E, Mikaeili A, Mohammadi P, Adibkia K. Preparation, physicochemical characterization and anti-fungal evaluation of the Nystatin-loaded Eudragit RS100/PLGA nanoparticles. Journal of Drug Delivery Science and Technology. 2017 2017/04/01/;38:90-6.
21. Justin C, Philip SA, Samrot AV. Synthesis and characterization of superparamagnetic iron-oxide nanoparticles (SPIONs) and utilization of SPIONs in X-ray imaging. Applied Nanoscience. 2017 2017/10/01;7(7):463-75.
22. Noqta OA, Sodipo BK, Aziz AA. One-pot synthesis of highly magnetic and stable citrate coated superparamagnetic iron oxide nanoparticles by modified coprecipitation method. Functional Composites and Structures. 2020;2(4):045005.
23. Saengruengrit C, Ritprajak P, Wanichwecharungruang S, Sharma A, Salvan G, Zahn DR, et al. The combined magnetic field and iron oxide-PLGA composite particles: Effective protein antigen delivery and immune stimulation in dendritic cells. Journal of colloid and interface science. 2018;520:101-11.
24. Panda J, Satapathy BS, Majumder S, Sarkar R, Mukherjee B, Tudu B. Engineered polymeric iron oxide nanoparticles as potential drug carrier for targeted delivery of docetaxel to breast cancer cells. Journal of Magnetism and Magnetic Materials. 2019;485:165-73.
25. Wang J, Liu J. PEI–folic acid modified carbon nanodots for cancer cell-targeted delivery and two-photon excitation imaging. RSC advances. 2016;6(24):19662-8.
26. Pandey S, Pandey P, Kumar R, Singh NP. Residual solvent determination by head space gas chromatography with flame ionization detector in omeprazole API. Brazilian Journal of Pharmaceutical Sciences. 2011;47(2):379-84.
27. Ferreira NN, Granja S, Boni FI, Prezotti FG, Ferreira LM, Cury BS, et al. Modulating chitosan-PLGA nanoparticle properties to design a co-delivery platform for glioblastoma therapy intended for nose-to-brain route. Drug Delivery and Translational Research. 2020;10(6):1729-47.
28. Nigam K, Kaur A, Tyagi A, Nematullah M, Khan F, Gabrani R, et al. Nose-to-brain delivery of lamotrigine-loaded PLGA nanoparticles. Drug Deliv Transl Res. 2019 Oct;9(5):879-90. PubMed PMID: 30887226. Epub 2019/03/20. eng.
29. Meng Q, Wang A, Hua H, Jiang Y, Wang Y, Mu H, et al. Intranasal delivery of Huperzine A to the brain using lactoferrin-conjugated N-trimethylated chitosan surface-modified PLGA nanoparticles for treatment of Alzheimer's disease. Int J Nanomedicine. 2018;13:705.
30. Teasdale A, Elder D, Nims RW. ICH quality guidelines: Wiley Online Library; 2017.
31. Ito T, Sun L, Bevan MA, Crooks RM. Comparison of nanoparticle size and electrophoretic mobility measurements using a carbon-nanotube-based coulter counter, dynamic light scattering, transmission electron microscopy, and phase analysis light scattering. Langmuir. 2004;20(16):6940-5.
32. Khlebtsov B, Khlebtsov N. On the measurement of gold nanoparticle sizes by the dynamic light scattering method. Colloid Journal. 2011;73(1):118-27.
33. Maity D, Kale S, Kaul-Ghanekar R, Xue J-M, Ding J. Studies of magnetite nanoparticles synthesized by thermal decomposition of iron (III) acetylacetonate in tri (ethylene glycol). Journal of Magnetism and magnetic Materials. 2009;321(19):3093-8.
34. Hachani R, Lowdell M, Birchall M, Hervault A, Mertz D, Begin-Colin S, et al. Polyol synthesis, functionalisation, and biocompatibility studies of superparamagnetic iron oxide nanoparticles as potential MRI contrast agents. Nanoscale. 2016;8(6):3278-87.

35. Iv M, Telischak N, Feng D, Holdsworth SJ, Yeom KW, Daldrup-Link HE. Clinical applications of iron oxide nanoparticles for magnetic resonance imaging of brain tumors. Nanomedicine. 2015;10(6):993-1018.
36. Na HB, Hyeon T. Nanostructured T1 MRI contrast agents. Journal of Materials Chemistry. 2009;19(35):6267-73.
37. Xiao S, Yu X, Zhang L, Zhang Y, Fan W, Sun T, et al. Synthesis of PEG-coated, ultrasmall, manganese-doped iron oxide nanoparticles with high relaxivity for T1/T2 dual-contrast magnetic resonance imaging. Int J Nanomedicine. 2019;14:8499.
38. Xiao N, Gu W, Wang H, Deng Y, Shi X, Ye L. T1–T2 dual-modal MRI of brain gliomas using PEGylated Gd-doped iron oxide nanoparticles. Journal of colloid and interface science. 2014;417:159-65.
39. Petran A, Radu T, Borodi G, Nan A, Suciu M, Turcu R. Effects of rare earth doping on multi-core iron oxide nanoparticles properties. Applied Surface Science. 2018;428:492-9.
40. Roy E, Patra S, Madhuri R, Sharma PK. Stimuli-responsive poly (N-isopropyl acrylamide)-co-tyrosine@ gadolinium: Iron oxide nanoparticle-based nanotheranostic for cancer diagnosis and treatment. Colloids and Surfaces B: Biointerfaces. 2016;142:248-58.
41. Jayanthi SA, Nathan DMGT, Jayashainy J, Sagayaraj P. A novel hydrothermal approach for synthesizing α-Fe2O3, γ-Fe2O3 and Fe3O4 mesoporous magnetic nanoparticles. Materials Chemistry and Physics. 2015;162:316-25.
42. Khan US, Manan A, Khan N, Mahmood A, Rahim A. Transformation mechanism of magnetite nanoparticles. Materials Science-Poland. 2015;33(2):278-85.
43. Serga V, Burve R, Maiorov M, Krumina A, Skaudžius R, Zarkov A, et al. Impact of gadolinium on the structure and magnetic properties of nanocrystalline powders of iron oxides produced by the extraction-pyrolytic method. Materials. 2020;13(18):4147.
44. Iqbal MZ, Ma X, Chen T, Ren W, Xiang L, Wu A. Silica-coated super-paramagnetic iron oxide nanoparticles (SPIONPs): a new type contrast agent of T 1 magnetic resonance imaging (MRI). Journal of Materials Chemistry B. 2015;3(26):5172-81.
45. Shah RR, Davis TP, Glover AL, Nikles DE, Brazel CS. Impact of magnetic field parameters and iron oxide nanoparticle properties on heat generation for use in magnetic hyperthermia. Journal of Magnetism and Magnetic Materials. 2015 2015/08/01/;387:96-106.
46. Cassim S, Giustini A, Petryk A, Strawbridge R, Hoopes P, editors. Iron oxide nanoparticle hyperthermia and radiation cancer treatment. Energy-based Treatment of Tissue and Assessment V; 2009: International Society for Optics and Photonics.
47. Ghasemian E, Vatanara A, Najafabadi AR, Rouini MR, Gilani K, Darabi M. Preparation, characterization and optimization of sildenafil citrate loaded PLGA nanoparticles by statistical factorial design. DARU Journal of Pharmaceutical Sciences. 2013;21(1):1-10.
48. Masserini M. Nanoparticles for brain drug delivery. International Scholarly Research Notices. 2013;2013.
49. Wang R, Degirmenci V, Xin H, Li Y, Wang L, Chen J, et al. PEI-Coated Fe3O4 nanoparticles enable efficient delivery of therapeutic siRNA targeting REST into glioblastoma cells. International journal of molecular sciences. 2018;19(8):2230.
50. Souza TG, Ciminelli VS, Mohallem NDS, editors. A comparison of TEM and DLS methods to characterize size distribution of ceramic nanoparticles. Journal of physics: conference series; 2016: IOP Publishing.
51. Song J-X, Yan Y, Yao J, Chen J-M, Lu T-B. Improving the solubility of lenalidomide via cocrystals. Crystal growth & design. 2014;14(6):3069-77.
52. Lancheros R, Guerrero CA, Godoy-Silva RD. Improvement of N-acetylcysteine loaded in PLGA nanoparticles by nanoprecipitation method. Journal of Nanotechnology. 2018;2018.
53. Agency EM, editor ICH guideline Q3C (R5) on impurities: guideline for Residual Solvents. Int Conf Harmon Tech Requir Regist Pharm Hum Use; 2015.

54. Zeng L, An L, Wu X. Modeling drug-carrier interaction in the drug release from nanocarriers. Journal of Drug Delivery. 2011;2011.
55. Segler A, Tsimberidou A-M. Lenalidomide in solid tumors. Cancer chemotherapy and pharmacology. 2012;69(6):1393-406.
56. Chiang WL, Ke CJ, Liao ZX, Chen SY, Chen FR, Tsai CY, et al. Pulsatile drug release from PLGA hollow microspheres by controlling the permeability of their walls with a magnetic field. Small. 2012;8(23):3584-8.
57. Fang K, Song L, Gu Z, Yang F, Zhang Y, Gu N. Magnetic field activated drug release system based on magnetic PLGA microspheres for chemo-thermal therapy. Colloids and Surfaces B: Biointerfaces. 2015;136:712-20.
58. Cui Y-n, Xu Q-x, Davoodi P, Wang D-p, Wang C-H. Enhanced intracellular delivery and controlled drug release of magnetic PLGA nanoparticles modified with transferrin. Acta Pharmacologica Sinica. 2017;38(6):943-53.
59. Gowthamarajan K, Singh SK. Dissolution testing for poorly soluble drugs: a continuing perspective. Dissolution Technologies. 2010;17(3):24-32.
60. Paarakh MP, Jose PA, Setty C, Christoper G. Release kinetics–concepts and applications. Int J Pharm Res Tech. 2018;8(1):12-20.
61. Yadav KS, Sawant KK. Modified nanoprecipitation method for preparation of cytarabine-loaded PLGA nanoparticles. Aaps Pharmscitech. 2010;11(3):1456-65.
62. Jain GK, Pathan SA, Akhter S, Ahmad N, Jain N, Talegaonkar S, et al. Mechanistic study of hydrolytic erosion and drug release behaviour of PLGA nanoparticles: Influence of chitosan. Polymer degradation and stability. 2010;95(12):2360-6.
63. Sharma S, Parmar A, Kori S, Sandhir R. PLGA-based nanoparticles: a new paradigm in biomedical applications. TrAC trends in analytical chemistry. 2016;80:30-40.
64. Morita TO, Yamaguchi A, Kimura S, Fujii H, Endo K, Izumi K, et al. Stability of lenalidomide suspension after preparation by a simple suspension method for enteral tube administration. Journal of Oncology Pharmacy Practice. 2016;22(4):579-83.